

## Chapter 2

# Modelling the formation of shoreface-connected sand ridges: dynamic coupling between mean currents and topography

A morphodynamic model is developed and analyzed to gain fundamental understanding on the basic physical mechanisms responsible for the characteristics of shoreface-connected sand ridges observed in some coastal seas.

Trowbridge (1995) studied the morphologic stability properties of a storm-driven alongshore current, with a cross-shore gradient, on a shelf bounded by a straight coast and with a transverse slope. His model consists of the 2D horizontal momentum equations and the mass conservation for the water motion, supplemented with a bottom evolution equation and a parametrization of the sediment transport. A severe assumption in this model is the condition of irrotational flow. This implies that production of vorticity due to bottom frictional torques and Coriolis terms, which has been proven to be very important for tidal sand banks dynamics (see Zimmerman 1981; Huthnance 1982; Hulscher *et al.* 1993) is neglected. In addition, a crude sediment transport parametrization is used, where the sediment flux is assumed to be linear in the mean flow velocity and the downslope effect on the transport direction is not accounted for. Despite these limitations, Trowbridge's model is able to predict the growth of topographic features similar in shape to the observed ones and with the correct orientation with respect to the current. The underlying physical mechanism is the offshore deflection of the flow over the shoals and the related loss of sediment carrying capacity in the offshore direction. The latter is due to the transverse bottom slope. However, as a result of the simplifications the model does not predict a preferred spacing between ridge crests. Furthermore, since the hydrodynamic equations are not solved, the offshore deflection of the flow, which is a key point of the model, is shown only by means of the approximate streamlines rather than by the exact flow.

In order to gain more fundamental knowledge on the dynamics of shoreface-connected sand ridges in this chapter is investigated a generalized and physically more realistic model for both the water and sediment motion. The fluid will be described by the full 2D shallow water equations, which include bottom friction and Coriolis terms. The sediment flux is assumed to be proportional to some power  $m$  of the current and the flux has a preferred down-slope component. The basic state of this model represents a steady longshore current, driven by wind and a pressure gradient, over longshore uniform bottom profile, with constant slope on the inner shelf and a horizontal bottom on the outer shelf. The dynamics of small perturbations on this state is analysed and they result controlled by three physical mechanisms. The first is the transverse bottom slope mechanism, associated to the seaward deflection of the current over the ridges and the loss of

---

This chapter is part of the paper *Modelling the formation of shoreface-connected sand ridges: dynamical coupling between long term averaged topography and current* under revision by the J.Fluid Mechanics, with co-authors A. Falqués and H. E. de Swart. Preliminary results appeared in Falqués, Calvete & Montoto (1998)

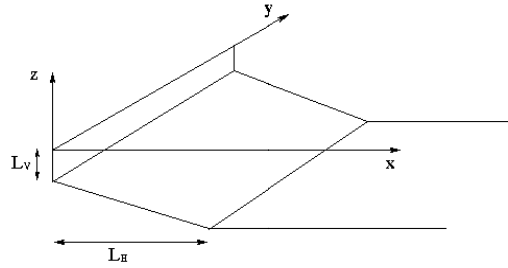


Figure 2.1: Sketch of the geometry and the coordinate system. For explanation of the symbols see the text.

sediment carrying capacity of a flow into deeper water. It is effective for  $1 \leq m \leq 1.05$  and yields the correct orientation, spacing and shape of the ridges, albeit the results are sensitive to the basic current profile. The two other instability mechanisms, which are only effective for  $m > 1$ , are related to vorticity production by bottom frictional and Coriolis torques. The bottom friction mechanism results in patterns of alternating shoals and pools whereas the Coriolis mechanism leads to elongated cyclonically rotated ridges. Comparison of the model results with field observations indicates that the ridge formation is mainly due to the transverse slope mechanism. Consequently, even in the presence of significant tidal currents, where these ridges could seem to be tidal sand banks distorted by the proximity of the coast (Dutch case, for instance), their origin is entirely different from that of tidal sand banks. The model also solves the hydrodynamic equations so that the perturbed flow related to each growing bottom disturbance is obtained. In this way the offshore deflection of the current over the ridges related to the transverse sloping bottom mechanism is reproduced.

In the next section the model equations and boundary conditions are formulated. Section 2.2 discusses the solution procedure. The results for the growth rates and spatial patterns of the bedforms in cases of a linear ( $m = 1$ ) and non-linear ( $m = 3$ ) sediment transport are investigated in section 2.3. An exploration for  $m$  varying between 1 and 3 is also performed. In section 2.4 the physical mechanisms within the model are discussed. Some concluding remarks are presented in the final section. Three appendixes complete this chapter, one on the effect of weather fluctuations, another with further details on the solution method and a third one presenting an analytical approximation of the transverse slope mechanism.

## 2.1 Model formulation

### 2.1.1 Equations of motion

As shown in figure 2.1, the inner shelf is schematized as a sloping sea bed, bounded by a straight vertical wall which represents the seaward end of the shoreface. Further offshore, a horizontal flat bottom describes the outer shelf. An orthogonal coordinate system is taken with the  $x$ ,  $y$  and  $z$ -axes pointing in the cross-shore, longshore direction and vertical direction, respectively. The still water level is represented by  $z = 0$ . Although the vertical structure of the currents can have an important role in the ridge area, in view of earlier studies on large scale bedforms (see the references mentioned in the introduction) it is worthwhile to investigate whether a 2D model can describe the main characteristics of the ridges. Therefore, the fluid motions are considered to be governed by the 2D shallow water equations, which consist of the depth-averaged momentum equation and mass conservation equation:

$$\frac{\partial \mathbf{v}}{\partial t} + (\mathbf{v} \cdot \nabla) \mathbf{v} + \mathbf{f}_c \times \mathbf{v} = -g \nabla z_s + \frac{\boldsymbol{\tau}}{\rho D} \quad (2.1)$$

$$\frac{\partial D}{\partial t} + \nabla \cdot (D \mathbf{v}) = 0 \quad (2.2)$$

Here  $\mathbf{v}$  is the current vector,  $\mathbf{f}_c \times \mathbf{v}$  is the Coriolis acceleration,  $\boldsymbol{\tau}$  represents the free surface and bottom stress terms ( $\boldsymbol{\tau} = \boldsymbol{\tau}_s - \boldsymbol{\tau}_b$ ) and  $\rho$  is the water density. In the momentum equations also

forcing terms due to wave-induced radiation stresses and horizontal momentum diffusion can be considered, but they will be neglected in the present study. The free surface, the bottom and the total height of the water column are given by  $z = z_s$ ,  $z = z_b$  and  $D$ , so that  $D = z_s - z_b$ . The nabla-operator is defined by  $\nabla = (\partial/\partial x, \partial/\partial y)$ . The bottom evolution follows from the sediment conservation equation:

$$\frac{\partial z_b}{\partial t} + \nabla \cdot \mathbf{q} = 0 \quad (2.3)$$

where  $\mathbf{q}$  denotes the volumetric sediment flux per unit width. It is important to note that, since the growth of the ridges takes place on very long time scales ( $O(10^3 \text{ yr})$ ), we are interested only in the averaged dynamics where the individual storm cycles have been filtered. Thus, all the governing equations in the model as well as all the quantities in them are assumed to be averaged over a time period longer than the time scale of a storm event. Since the instantaneous governing equations are non-linear, there would be a contribution from the fluctuations into the averaged equations. This contribution has been neglected in the present model. However, these concepts are sketched in appendix A in order to illustrate the complications and some of the implications of taking fluctuations into account.

The boundary conditions imposed for this system are periodic conditions in the longshore direction. Furthermore, at  $x = 0$  (the transition shoreface-inner shelf) and for  $x \rightarrow \infty$  we assume that the cross-shore flow component vanishes and the bottom elevation is fixed to its reference value. These conditions are motivated by the fact that the ridges are trapped into the inner shelf. Therefore, the bottom elevation must vanish far offshore and near the shoreface. The cross-shore flow must vanish far off-shore for the same reason. The vanishing cross-shore flow component at  $x = 0$  is based on the assumption that exchange processes between inner shelf and shoreface can be neglected. Notice that the condition of vanishing perturbations far offshore is consistent with the fact that we are looking for inherent instabilities of the inner shelf rather than forced behaviour driven by offshore features.

In order to close the model parametrizations for the bed shear stress  $\tau_b$  and the sediment flux  $\mathbf{q}$  are required. We will consider both a linear friction law

$$\tau_b = \rho r_* \mathbf{u} \quad (2.4)$$

and a quadratic friction law

$$\tau_b = \rho c_d |\mathbf{u}| \mathbf{u}$$

with  $r_*$  a friction coefficient and  $c_d$  a drag coefficient. The volumetric sediment flux is parametrized as

$$\mathbf{q} = \nu |\mathbf{v}|^m \left( \frac{\mathbf{v}}{|\mathbf{v}|} - \gamma \nabla h \right)$$

Here  $\nu$  is a coefficient which depends on the wave stirring and on the sediment properties and bed porosity. Wave stirring depends on wave height and water depth through wave orbital velocity near the bottom (see appendix A, equation (A.3),  $\nu = \nu_0 |\mathbf{v}''|^{b-1}$ ), which of course, has cross-shore gradients. For simplicity, we will hereafter assume that it is constant. The implications of such an assumption will be briefly discussed in section 2.5. Furthermore,  $\gamma$  is the Coulomb (friction) coefficient (of order 1) related to the angle of repose of the sediment and  $m$  is an exponent which is usually between 1 and 6. Finally,  $h$  is the elevation of the bottom with respect to a specific equilibrium profile, to be discussed in the next subsection. The term  $-\gamma \nabla h$  accounts for the tendency of sand to move downslope. Further details on sediment transport can be found in Van Rijn (1993) and Fredsoe & Deigaard (1993).

### 2.1.2 Basic state and stability analysis

Field observations of the bathymetry of the inner shelf indicate that the mean bottom profile (i.e., averaged in the longshore direction) is characterized by a nearly constant slope  $\beta_*$ , which is typically of order  $10^{-4} - 10^{-3}$ . The slope of the outer shelf is considerably smaller. In this study we model the reference bottom profile as

$$H(x) = \begin{cases} L_V + \beta_* x & (0 \leq x < L_H) \\ H_{os} & (x \geq L_H) \end{cases} \quad (2.5)$$

Here  $L_V$  is the water depth at the transition shoreface-inner shelf,  $L_H$  is the width of the inner shelf and  $H_{os}$  the water depth on the outer shelf. For example, representative values for the Dutch inner shelf are  $L_V \sim 15$  m,  $L_H \sim 12 \times 10^3$  m,  $H_{os} \sim 20$  m, so  $\beta_* \equiv (H_{os} - L_V)/L_H \sim 4 \times 10^{-4}$ .

Now, we will consider the possibility of a mean longshore current with a cross-shore gradient,  $V(x)$ , which is driven by the mean alongshore wind stress  $\tau_{sy}$  and the mean longshore gradient in the free surface elevation,  $s$ , both assumed to be uniform. This would mean a basic steady state of the form

$$\mathbf{v} = (0, V(x)) \quad z_s = sy + \xi(x) \quad z_b = -H(x)$$

and the momentum equations would then read

$$f_c V = g \frac{d\xi}{dx}, \quad 0 = -gs + \frac{(\tau_{sy} - \tau_{by})}{\rho D} \quad (2.6)$$

However, the total depth,  $D = H(x) + sy + \xi(x)$ , would introduce a dependence on the alongshore coordinate in the second equation (2.6). According to observations, the deformation of the mean free surface is much smaller than the depth below still water level, i.e.  $|sy + \xi(x)| \ll |H(x)|$ . This allows us to approximate  $D$  by  $H$  in this equation so that the  $y$ -dependence becomes negligible. Consequently, a velocity profile given by

$$V = \frac{\tau_{sy}/\rho - gsH}{r_*} \quad (2.7)$$

in case of a linear friction law, and

$$V = \pm \left| \frac{\tau_{sy}/\rho - gsH}{c_d} \right|^{1/2} \quad (2.8)$$

in case of a quadratic friction law, would achieve approximately the alongshore momentum balance between forces related to the longshore pressure gradient, windstress and bottom friction, respectively. The sign of the velocity is determined by the direction of the windstress and of the pressure gradient force. The consistency of the assumption  $D \simeq H$  can be checked as follows. From the cross-shore balance (equation 2.6), since  $V \sim 1$  m s<sup>-1</sup> and  $\Delta x \sim 10^4$  m, the setup/setdown due to Coriolis can be estimated to be less than  $\sim 0.1$  m, that is, much smaller than  $H \sim 15$  m. Furthermore, according to observations (Scott & Csanady, 1976; Chase, 1979), the longshore gradient in the sea surface elevation does not exceed  $\sim 10^{-6}$ , which over a distance of  $\Delta y \sim 100$  km, would make  $\Delta z_s \sim 0.1$  m. As we will see, even though  $s$  is negligible for the total depth evaluation, the associated pressure gradient force is comparable to the force due to the wind stress and will therefore be retained in (2.7), (2.8). The mass conservation equation is verified identically and, since  $h = 0$ , the sediment flux is directed alongshore and there are no spatial divergences in the transport.

It has been demonstrated by Scott & Csanady (1976) and by Van der Giessen, De Ruijter & Borst (1990) that the momentum balances in equation (2.6) using the linear friction law (2.4) yield a good description of mean currents in the coastal zone. Analysis of current data obtained on the East American inner shelf (Scott & Csanady 1976; see also Chase 1979) indicate that the sea surface slope  $s \sim 1 - 2 \times 10^{-7}$  and the friction coefficient  $r_* \sim 5 \times 10^{-4}$  m s<sup>-1</sup>. The corresponding drag coefficient of the bottom is  $c_d \simeq 0.002$ . Similar values appear to apply to the Dutch inner shelf. The physical mechanism causing the longshore pressure gradient is discussed by Chase (1979).

Instead of using analytical profiles, observed current structures over the inner shelf can be used, but unfortunately data are scarce. Results for the East American shelf (near Long Island) are presented in Niedoroda & Swift (1981) and Niedoroda, Swift, Hopkins & Ma (1984), see also Niedoroda & Swift (1991) for a review. Results for the coast of Nova Scotia are reported by Thompson & Sheng (1997). During storm conditions depth-averaged currents tend to increase with increasing offshore distance and decay for depths larger than 15m. Comparison with the analytical profiles suggest that the longshore pressure gradient is indeed important for the maintenance of the flow. As the main aim of the present paper is to model and understand the formation of shoreface-connected ridges, our basic state should be representative of the long term averaged situation. This

long term average may be quite uncertain but it seems clear that both forcings, wind stresses and pressure gradients, should be considered.

Based on the field data discussed above we choose  $\tau_{sy} \simeq -0.1 \text{ Nm}^{-2}$  and  $s \simeq 2 \times 10^{-7}$ . This yields an estimate of the longshore velocity scale:  $U \equiv V(x=0) \simeq 0.25 \text{ ms}^{-1}$ . This implies that both the longshore windstress and pressure gradient force a flow in the same, negative,  $y$ -direction. However, we will also investigate the effect of reversing the flow direction while keeping the profile fixed. Note that with this choice of wind stress we have  $\tau/\rho \sim 10^{-4} \text{ m}^2 \text{ s}^{-2}$  while  $gsH \sim 2.10^{-4} \text{ m}^2 \text{ s}^{-2}$ , so that both terms in equation (2.7) are comparable. The formation of rhythmic bedforms can then be investigated by studying the dynamics of small perturbations evolving on this steady state:

$$\mathbf{v} = (0, V) + (u(x, y, t), v(x, y, t))$$

$$z_s = \zeta + \eta(x, y, t) \qquad z_b = -H + h(x, y, t)$$

where  $\zeta = sy + \xi(x)$ . The resulting equations of motion for the perturbations will be presented in the next subsection.

### 2.1.3 Scaling and linearized model

In order to make the equations of motion dimensionless we now introduce characteristic magnitudes  $L_H$ ,  $U$  and  $L_V$  for the horizontal length, the longshore current and the depth. These scales have been defined in the previous subsection. Then two time scales appear in a natural way which are defined as

$$T_h = \frac{L_H}{U} \qquad T_m = \frac{L_H L_V}{\nu U^m}$$

The hydrodynamic time scale  $T_h$  follows from scaling the three equations (2.1)–(2.2) and the morphodynamic time scale  $T_m$  results from scaling equation (2.3). The variables are made dimensionless as follows:

$$(x, y) = L_H(x', y') \qquad t = T_m t' \qquad \mathbf{v} = U \mathbf{v}' \qquad z_b = L_V z'_b \qquad z_s = \frac{U^2}{g} z'_s$$

The scaled linearized momentum (2.1) and mass conservation equation (2.2) read:

$$\epsilon \frac{\partial u}{\partial t} + V \frac{\partial u}{\partial y} - \hat{f}v = -\frac{\partial \eta}{\partial x} - \frac{r_1}{D_0} u \qquad (2.9a)$$

$$\epsilon \frac{\partial v}{\partial t} + V \frac{\partial v}{\partial y} + \frac{dV}{dx} u + \hat{f}u = -\frac{\partial \eta}{\partial y} - \frac{r_2}{D_0} v - \delta \frac{(F^2 \eta - h)}{D_0} \qquad (2.9b)$$

$$\epsilon \frac{\partial (F^2 \eta - h)}{\partial t} + \frac{dD_0}{dx} u + D_0 \frac{\partial u}{\partial x} + D_0 \frac{\partial v}{\partial y} + V \frac{\partial (F^2 \eta - h)}{\partial y} = 0 \qquad (2.10)$$

where  $D_0 = F^2 \zeta + H$ , and the sediment conservation equation (2.3) reads:

$$\begin{aligned} \frac{\partial h}{\partial t} = -|V|^{m-1} & \left\{ \frac{(m-1)}{V} \frac{dV}{dx} u + \frac{\partial u}{\partial x} + m \frac{\partial v}{\partial y} \right. \\ & \left. - \hat{\gamma} |V| \left( \frac{m}{V} \frac{dV}{dx} \frac{\partial h}{\partial x} + \frac{\partial^2 h}{\partial x^2} + \frac{\partial^2 h}{\partial y^2} \right) \right\} \end{aligned} \qquad (2.11)$$

Note that from now on  $V$  is a nondimensional reference velocity. The parameters in the model are

$$\epsilon = \frac{T_h}{T_m} \qquad \delta = \frac{gsL_H}{U^2} \qquad \hat{\gamma} = \gamma \frac{L_V}{L_H}$$

$$F^2 = \frac{U^2}{gL_V} \qquad \hat{f} = \frac{f_c L_H}{U}$$

and

$$r_1 = r_2 \equiv r = r_* L_H / UL_V \quad (\text{linear friction})$$

$$r_1 = \frac{1}{2} r_2 \equiv r|V| = c_d |V| L_H / L_V \quad (\text{quadratic friction})$$

For convenience, the primes have been dropped. The Coriolis parameter is the inverse of the Rossby number,  $\hat{f} = Ro^{-1}$ . It has been assumed that  $c_d U = r_*$  which means that in equilibrium the energy dissipation due to quadratic bottom friction equals that induced by a linear bottom friction. Furthermore, the hydrodynamic timescale is assumed to be much smaller than the morphodynamic one. This allows for the adoption of the quasi-steady hypothesis, that is, the fluid instantaneously adjusts to the bathymetric changes. This permits to drop the time derivatives ( $\epsilon \approx 0$ ) in the three linear differential equations (2.9)–(2.10). Furthermore, using the scales of motion discussed in section 2.1.2, it appears that the Froude number  $F$  is very small,  $F \sim 0.02$ . Consequently, in the forthcoming analysis terms proportional to  $F^2$  will be neglected as well. This is consistent with the choice of our reference state, which only exists for low Froude numbers.

The corresponding boundary conditions are periodic conditions in the longshore direction and furthermore  $u = 0$  and  $h = 0$  both at  $x = 0$  and for  $x \rightarrow \infty$ .

## 2.2 Solution procedure

The procedure to solve the model equations is as follows. The equations (2.9)–(2.11) allow for alongshore travelling and growing wave solutions with an as yet unknown cross-shore structure. Thus we consider perturbations of the form

$$(u, v, \eta, h) = \text{Re}\{(\hat{u}(x), \hat{v}(x), \hat{\eta}(x), \hat{h}(x))e^{iky+\omega t}\}$$

Here  $k$  is the wavenumber and  $\omega$  a complex frequency. The real part,  $\text{Re}(\omega)$ , denotes the growth rate of the perturbation and  $-\text{Im}(\omega)$  the frequency. Instability occurs if  $\text{Re}(\omega)$  is positive: then the mode grows exponentially in time. The part which describes the bottom is called a topographic wave. As a result equations (2.9)–(2.10), dropping hats for convenience, reduce to:

$$\begin{pmatrix} ikV + r_1/H & -\hat{f} & \frac{d}{dx} \\ \frac{dV}{dx} + \hat{f} & ikV + r_2/H & ik \\ \frac{dH}{dx} + H\frac{d}{dx} & ikH & 0 \end{pmatrix} \begin{pmatrix} u \\ v \\ \eta \end{pmatrix} = \begin{pmatrix} 0 \\ \delta/H \\ ikV \end{pmatrix} h \quad (2.12)$$

and equation (2.11) becomes:

$$\omega h = -|V|^{m-1} \left\{ \frac{(m-1)}{V} \frac{dV}{dx} u + \frac{du}{dx} + ikmv - \hat{\gamma}|V| \left( \frac{m}{V} \frac{dV}{dx} \frac{dh}{dx} + \frac{d^2 h}{dx^2} - k^2 h \right) \right\} \quad (2.13)$$

The first step is to solve equations (2.12) for  $u$ ,  $v$  and  $\eta$  for a given bottom perturbation  $h$ . This problem will hereafter be called *the flow over topography problem* (FOT). Physically, this means finding the response of the flow to a given perturbation on the sea bed. Since equations (2.12) are linear in  $u$ ,  $v$ ,  $\eta$ , solving the FOT problem defines three linear integro-differential operators  $\mathbf{U}$ ,  $\mathbf{V}$ ,  $\mathbf{E}$  such that

$$u(x) = [\mathbf{U}h](x) \quad v(x) = [\mathbf{V}h](x) \quad \eta(x) = [\mathbf{E}h](x) \quad (2.14)$$

The second step is to substitute the results (2.14) into the bottom evolution equation (2.13). Together with the boundary conditions, which are discussed in the previous section, this defines an eigenvalue problem of the form

$$\omega h = \mathbf{B}h \quad (2.15)$$

where  $\omega$  is the eigenvalue and  $h(x)$  the eigenfunction and where the linear operator  $\mathbf{B}$  is a combination of  $\mathbf{U}$  and  $\mathbf{V}$ . Expressions for these operators are presented in appendix B. The solutions are obtained numerically by the application of spectral methods, for details see Falqués *et al.* (1996) and references therein. The numerical model which solves this problem is called MORFO20.

## 2.3 Model Results

### 2.3.1 Basic state and parameter values

In this section the results obtained with the numerical model will be presented. In order to fit our model to the situation on the Dutch inner shelf, we choose values for the parameters  $L_V, L_H, \beta_*, U, r_*, c_d$  and  $s$  as discussed in section 2.1.2. Here, a default value  $\gamma = 0.08$  will be adopted for the Coulomb coefficient in the sediment flux. As it will be shown, the model prediction of the ridge spacing depends largely on  $\gamma$  and this is the value that gives the best fit with the Dutch coast observations. The validity of this choice according to experimental values will be discussed in section 2.5. The Dutch coast is at a latitude of  $51^\circ\text{N}$ , thus the Coriolis parameter is  $f_c = 1.12 \times 10^{-4} \text{ s}^{-1}$ . Consequently, the default values of the non-dimensional parameters in our study are

$$r = 1.5 \qquad \hat{f} = 5.35 \qquad \hat{\gamma} = 1 \times 10^{-4} \qquad \delta = 0.35$$

The nondimensional bathymetry reads

$$H(x) = \begin{cases} 1 + \beta x & \text{if } 0 \leq x \leq 1 \\ 1 + \beta & \text{if } x > 1 \end{cases} \quad (2.16)$$

as is derived from equation (2.5), and  $\beta=1/3$ . The corresponding velocity profile then follows from either equation (2.7) or (2.8), depending on the parametrization of the bottom shear stress. For example, in case of the linear friction law the result becomes

$$V(x) = \begin{cases} \pm(1 + a\beta x) & \text{if } 0 \leq x \leq 1 \\ \pm(1 + a\beta) & \text{if } x > 1 \end{cases}$$

and the sign of the flow is determined by the direction of the applied wind and longshore pressure gradient forces. Note that parameter  $\delta$  is negative in case  $V > 0$  because the sign of the longshore pressure gradient changes sign in that case. The parameter  $a = |\delta|/r \simeq 0.23$  measures the relative effect of the longshore pressure gradient in maintaining the basic state velocity and can be written as  $a = g|s|L_v/(r_*U)$ . By using the definition of velocity scale  $U$  it follows that  $a$  can vary between 0 (no pressure gradient) and 1 (windstress negligible).

In this study we will focus on the dynamics of bedforms in the case where the current has the coast to the right in the Northern Hemisphere ( $\hat{f} > 0, V < 0$ ), which is the case of the Dutch and the North American coasts. On the Argentinian shelf the current is directed to the north ( $V > 0$  in the present model) but then,  $\hat{f} < 0$ . However, the latter situation is equivalent to the former one because the system has a mirror symmetry with respect to the  $y = 0$  plane. Indeed, given a current profile  $V(x)$  and a value of the Coriolis parameter,  $\hat{f}$ , from any solution of the linearized governing equations  $u(x, y, t)$ ,  $v(x, y, t)$ ,  $\eta(x, y, t)$  and  $h(x, y, t)$  (equations (2.1), (2.2) and (2.3)) a solution for  $V^* = -V(x)$  and  $\hat{f}^* = -\hat{f}$  can be obtained just by making

$$\begin{aligned} u^*(x, y, t) &= u(x, -y, t) & v^*(x, y, t) &= -v(x, -y, t) \\ \eta^*(x, y, t) &= \eta(x, -y, t) & h^*(x, y, t) &= h(x, -y, t). \end{aligned}$$

Therefore, there are only two independent situations,  $\hat{f}V < 0$  and  $\hat{f}V > 0$ . Some results for the latter case will also be presented when discussing the effect of Coriolis force.

### 2.3.2 Linear sediment transport, $m=1$ , and linear friction

In this subsection a sediment transport proportional to the current is considered, i.e.,  $m = 1$ . This choice is representative for situations that the wave-induced orbital velocity near the bed is much larger than the steady current. The sediment is then stirred by the waves and subsequently transported by the current. As stated in section 2.1.1, the cross-shore variations of the intensity of this stirring have been neglected in the present model. For reasons of consistency this also implies that a linearized bed shear stress for the steady current is adopted. In the next subsections higher values of  $m$  will be considered in combination with a quadratic bottom friction law. A physical interpretation of the results will be given in section 2.4.

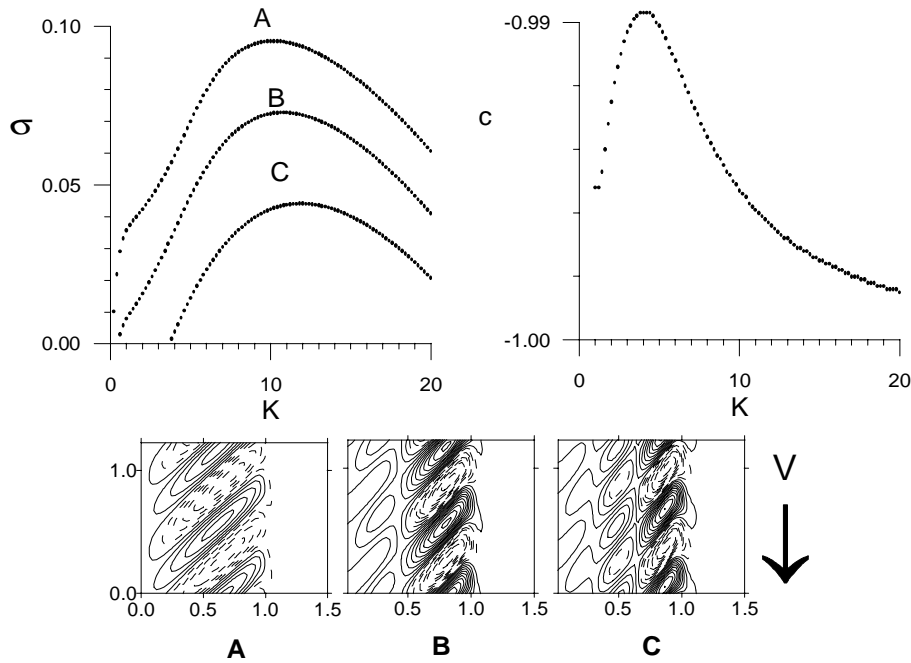


Figure 2.2: Nondimensional growth rate,  $\sigma = \text{Re}(\omega)$ , and phase speed  $c = -\text{Im}(\omega)/k$  as a function of the wavenumber,  $k$ , for the first three modes (upper part). Parameter values are  $m = 1$ ,  $a = 1$ ,  $r = 1.5$ ,  $\hat{f} = 5.35$ ,  $\hat{\gamma} = 10^{-4}$ ,  $\beta = 0.33$  and  $V < 0$ . The contour plots of the three bottom modes with the largest growth rate, are shown below. Shoals and pools are indicated by continuous and dashed lines, respectively. In each plot the  $y$  axis (vertical on the left) represents the shoreface and the  $x > 0$  axis (horizontal on the bottom) the inner shelf. The direction of the basic current is shown by a big arrow. Note the upcurrent rotation of the ridges.

The model will be analyzed using the basic state solution and parameter values discussed in section 2.3.1. However in the first series of experiments the parameters  $\delta$  and  $a$  will be varied while keeping their ratio  $\delta/r \equiv a$  fixed. Physically this means that both the longshore windstress and pressure gradient are varied, without changing the velocity scale  $U$ . In figure 2.2 curves are presented of the growth rates of the first three eigenmodes for  $a = 1$ . In this case the basic state current is fully determined by the longshore pressure gradient. Note that the ratio  $V/H$  is constant, as was also studied by Trowbridge (1995). An important difference is that in the present model the preferred downslope movement of the sediment is accounted for. This causes the growth rate to have a maximum for  $k \simeq 10$ , which corresponds to a spacing of about 7 km. This agrees with the observed spacings of shoreface-connected sand ridges on the Dutch inner shelf (Van de Meene, 1994). The corresponding phase speeds are  $c \simeq -1$  and this variable shows almost no dependence on  $k$ . This means that ridges behaves like topographic waves which migrate downcurrent with a celerity  $V_{mi} \simeq L_H/T_m$ . In view of the fact that the maximum growth rate is  $\text{Re}(\omega) \simeq 0.1$ , the amplitude of the dominant bottom mode grows approximately 6% during the period that the perturbation travels one wave-length. An estimate of the characteristic growth time (e-folding time) can be obtained from the horizontal lengthscale,  $L_H \sim 12$  km and a typical migration speed,  $V_{mi} \sim 4$  m yr $^{-1}$ , by means of

$$\tau = \frac{L_H}{V_{mi}} \frac{c}{\text{Re}(\omega)}$$

This yields  $\tau \sim 3 \times 10^4$  yr. The shape of the modelled ridges are shown in figure 2.2b. This is done for the wavenumbers which correspond to maxima in the three different growth rate curves. Clearly, the orientation of the dominant bedforms is such that they are upcurrent rotated: the seaward ends of the crests are shifted upstream with respect to their shoreface attachments. This agrees well with the observed orientation of the four ridge patches discussed in the introduction. Figure 2.3 shows the contour plot of mode 1 in figure 2.2 along with the corresponding perturbation on the current. The offshore deflection of the current over the crests and the onshore deflection over

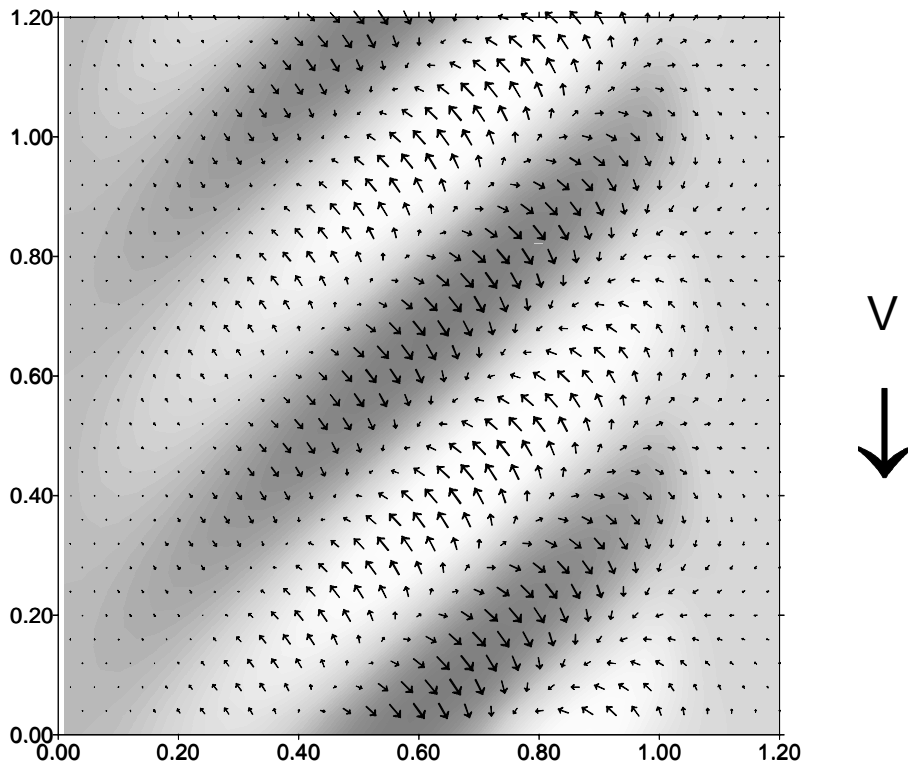


Figure 2.3: Contour plot of the first mode in figure 2.2 with the associated perturbation of the current indicated by arrows. Shoals and pools are indicated by dark and white colours, respectively. Note the offshore current deflection over the crests.

the troughs can be seen, as well as the acceleration of the flow over the crests and the deceleration over the troughs.

In figures 2.4, 2.5 and 2.6 growth rate curves are shown for  $a = 0.9$ ,  $a = 0.8$  and  $a = 0.6$ , respectively. Results for the phase speeds are not presented, because they hardly differ from the case  $a = 1$ . Now the longshore windstress contributes to the maintenance of the basic current profile and hence the ratio  $V/H$  is no longer constant. This leads to substantial differences compared with the case that  $a = 1$ . First of all the wavenumber of the dominant mode becomes much smaller:  $k_m \sim 7$  for  $a = 0.8$  and  $k_m \sim 1$  for  $a = 0.6$ . Obviously, the predicted ridge spacings become much larger than those observed in the field. Besides, the growth rates decrease with decreasing  $a$  and hence the  $e$ -folding time scale of the bedforms becomes unrealistically large. Another interesting aspect in figure 2.5 is the competition between different dominant modenumbers. Clearly, the mode which is dominant in case  $a = 1$  is overtaken by a new mode if  $a = 0.8$ . The latter mode has two local maxima in its growth rate curve. For  $a$  close to 1 its dominant wavenumber is close to 7, but with decreasing  $a$  this role is taken over by a much lower wavenumber. The bottom contours corresponding to the peaks in the instability curves are also shown. It appears that these modes all have a different spatial structure. The main differences are that some of them are attached to the shoreface while some are not. Sometimes they appear to be very elongated. On the other hand, a striking overall characteristic of all modes is the upcurrent orientation of their crests.

The dependence of the growth rates on the transverse bed slope  $\beta$  is shown in figure 2.7 for  $a = 1$  and all other parameters default. The transverse bed slope,  $\beta$ , and the Coulomb coefficient,  $\hat{\gamma}$ , have a significant effect on growth rates. The latter increase monotonically with increasing  $\beta$  but the characteristics of the preferred modes do not change. In contrast, increasing  $\hat{\gamma}$  leads to smaller growth rates and the wavenumber of the most preferred mode shifts to smaller values. If  $\hat{\gamma}$  becomes larger than about  $8 \times 10^{-4}$  instabilities no longer exist.

The effect of earth rotation on the instability mechanism has been investigated by carrying out experiments with all parameters having their default values but for  $a = 1$  and different values of the Coriolis parameter:  $\hat{f} = 0, 7, -7$ . The latter are representative for an inner shelf which is located

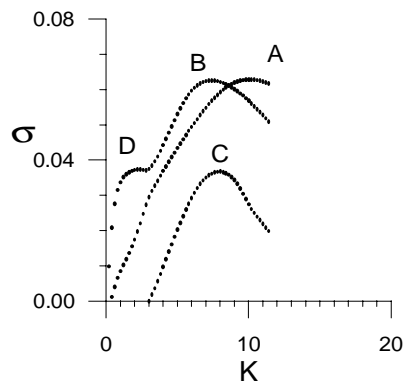


Figure 2.4: Growth rate curves as a function of the wavenumber for  $a = 0.9$  and the other parameter values are  $m = 1$ ,  $r = 1.5$ ,  $\hat{f} = 5.35$ ,  $\hat{\gamma} = 10^{-4}$ ,  $\beta = 0.33$  and  $V < 0$ . The corresponding bottom contours of the first three modes are also shown; the letters refer to the location in the growth rate plot.

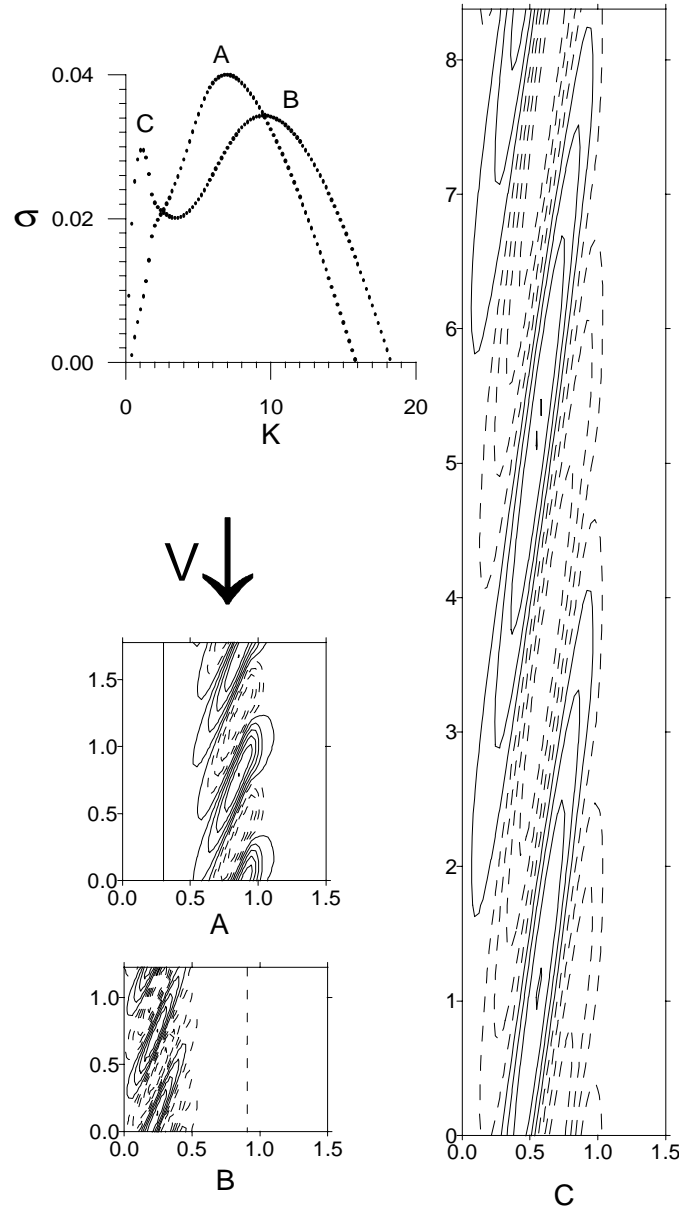


Figure 2.5: Growth rate curves as a function of the wavenumber for  $a = 0.8$  and the other parameter values are  $m = 1$ ,  $r = 1.5$ ,  $\hat{f} = 5.35$ ,  $\hat{\gamma} = 10^{-4}$ ,  $\beta = 0.33$  and  $V < 0$ . Corresponding bottom contours are also shown; the letters refer to the location in the growth rate plot.

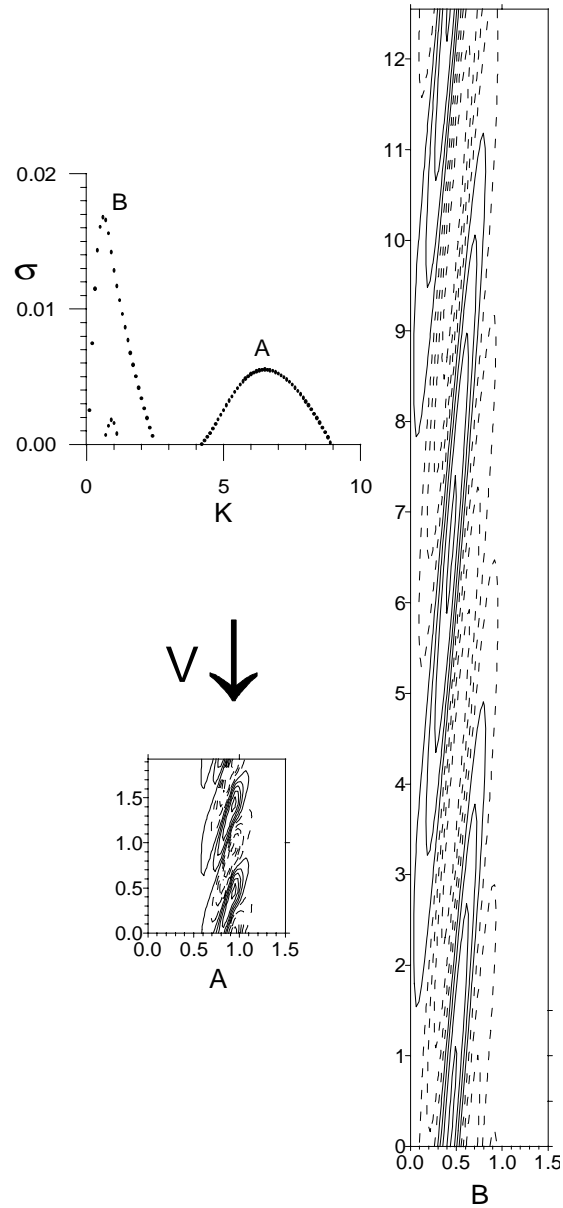


Figure 2.6: Growth rate curves as a function of the wavenumber for  $a = 0.6$  and the other parameter values are  $m = 1$ ,  $r = 1.5$ ,  $\hat{f} = 5.35$ ,  $\hat{\gamma} = 10^{-4}$ ,  $\beta = 0.33$  and  $V < 0$ . Corresponding bottom contours are also shown; the letters refer to the location in the growth rate plot.

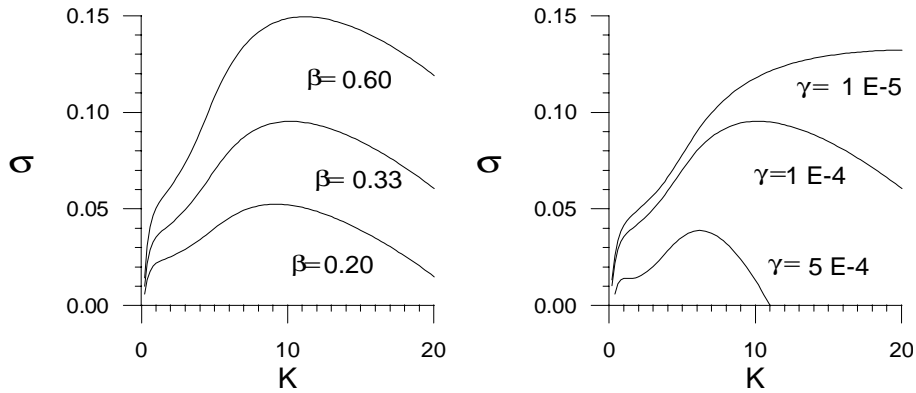


Figure 2.7: Growth rate curves of the first mode for different values of the transverse bottom slope coefficient  $\beta$  (left) and for different values of the Coulomb coefficient  $\hat{\gamma}$  (right). All other parameter values are  $m = 1$ ,  $a = 1$ ,  $r = 1.5$ ,  $\hat{f} = 5.35$ ,  $\hat{\gamma} = 10^{-4}$ ,  $\beta = 0.33$  and  $V < 0$ .

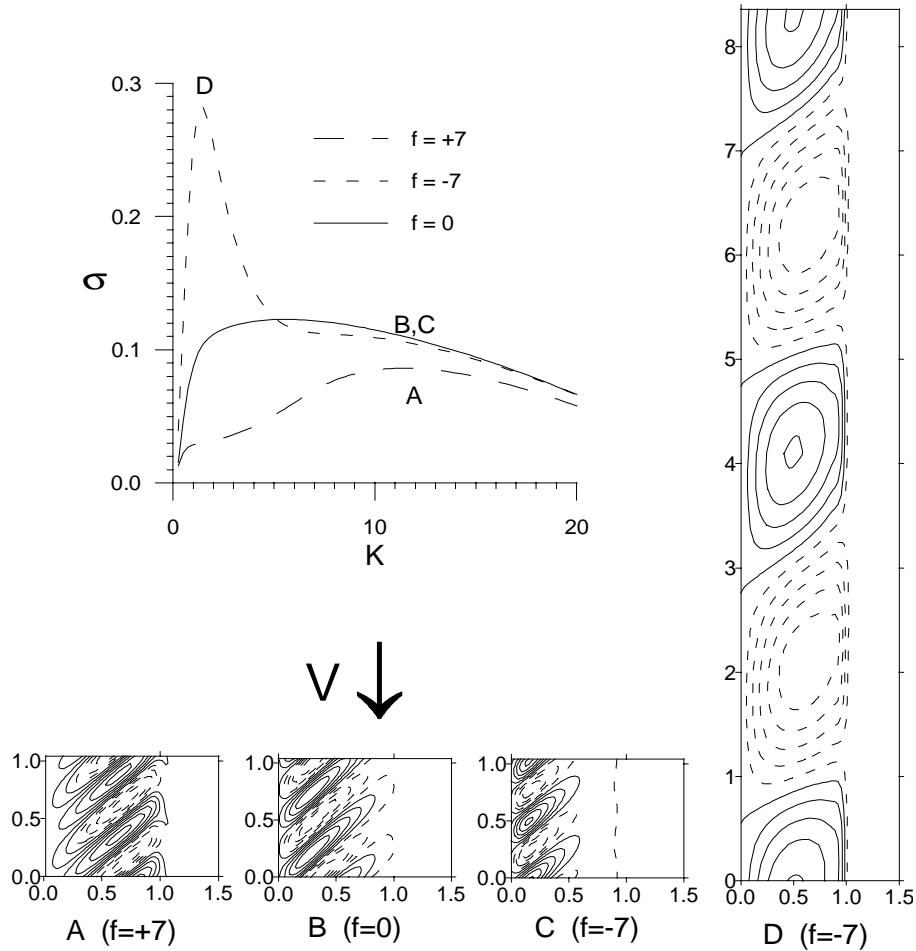


Figure 2.8: Growth rate curves of the first mode for different values of the Coriolis parameter  $\hat{f}$ . All other parameter values are  $m = 1$ ,  $a = 1$ ,  $r = 1.5$ ,  $\hat{\gamma} = 10^{-4}$ ,  $\beta = 0.33$  and  $V < 0$ . The bottom contours are also shown, for  $k = 12$  (A,B,C) and for the peak at  $k = 1.5$  (D).

at the equator, the North pole and the South pole, respectively. The results, shown in figure 2.8, indicate that earth rotation hardly affects the topographic waves which have wavenumbers  $k \sim 10$ . In this regime, Coriolis force produces just an inshore shift of the ridges (C) in the Southern

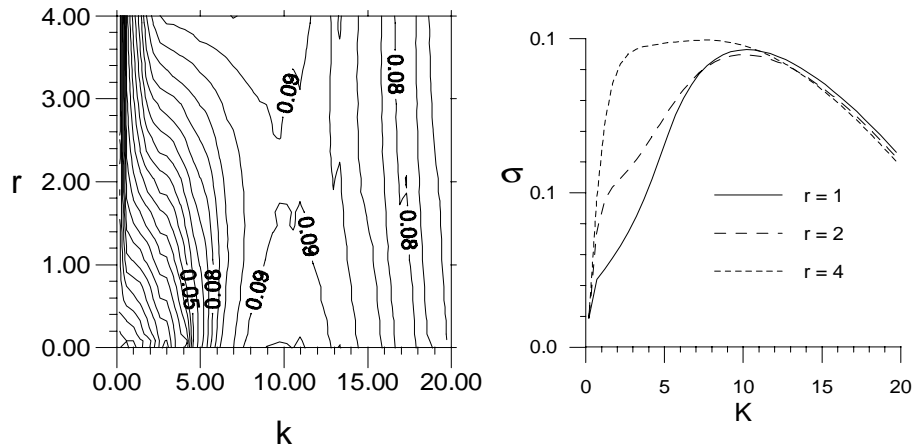


Figure 2.9: Curves of constant growth rate of the first mode as a function of wavenumber  $k$  and friction parameter  $r$  (left). Growth rate curves for different fixed values of  $r$  (right). A linear bottom friction law is adopted and parameter values are  $m = 1$ ,  $a = 1$ ,  $r = 1.5$ ,  $\hat{f} = 5.35$ ,  $\hat{\gamma} = 10^{-4}$ ,  $\beta = 0.33$  and  $V < 0$ .

Hemisphere and an offshore shift in the Northern Hemisphere (A) along with a slight inhibition of the instability in the latter case. In contrast, earth rotation has a strong influence on long topographic waves, making the instability mechanism to be much more effective on the Southern Hemisphere. In this case, a sharp peak in the growth rate curve occurs for very long wave-lengths. The corresponding bedforms show a little obliquity with respect to the coast and differ substantially from the observed elongated ridges (D).

Finally the sensitivity of the model results to the friction parameter has been investigated. Figure 2.9 shows the growth rates of the most dominant mode as a function of the wavenumber  $k$  for various values of parameter  $r$ . Here  $a = 1$  and all other parameters have their default values. The general trend appears to be that growth rates increase with increasing  $r$ , in particular for relatively small wavenumbers ( $k < 8$ ). However, for  $k$  around 10 or larger, the growth rates hardly depend on  $r$ . Furthermore, the wavenumber for which the instability mechanism is most effective become smaller if the friction parameter is increased. Apart from a longer wave-length the spatial characteristics of the preferred bottom modes (not shown) do not change significantly.

We end this subsection with some remarks on the reliability of the numerical solutions of our model equations. It is well-known that numerical solutions of eigenvalue problems can lead to spectral pollution, i.e., to the appearance of spurious solutions (Falqués *et al.*, 1996). The latter can be recognized by large variations of the eigenvalues if the number of freedom degrees of the discretization,  $N$ , is increased. Approximations to a true physical solution must converge when  $N$  is increased. This numerical convergence is clearly found in case that  $m = 1$  without any special conditions on the current profile: dominant eigenvalues computed with  $N = 60$  or with  $N = 120$  differ less than 0.05%.

### 2.3.3 Cubic sediment transport, $m=3$ , and nonlinear friction

In this section we will investigate the model with a different exponent in the parametrization of the sediment flux, i.e.,  $m = 3$ . Thus it is assumed that the transport is a cubic function of the mean velocity. This choice applies to a situation in which the wave orbital velocity and tidal velocity near the bed are small compared to the steady current. Hence the latter accounts for both the stirring and the transport of the sediment. A similar transport law was used by e.g. Schielen *et al.* (1993) and Hulscher *et al.* (1993). The basic state solution and parameter values are representative for the Dutch inner shelf and can be found in section 2.3.1.

First we investigate the model behaviour for the following current profile:

$$V(x) = \begin{cases} -[1 + a\beta x]^{\frac{1}{2}} \exp(-bx) & \text{if } 0 \leq x \leq 1 \\ -[1 + a\beta]^{\frac{1}{2}} \exp(-bx) & \text{if } x \geq 1 \end{cases}$$

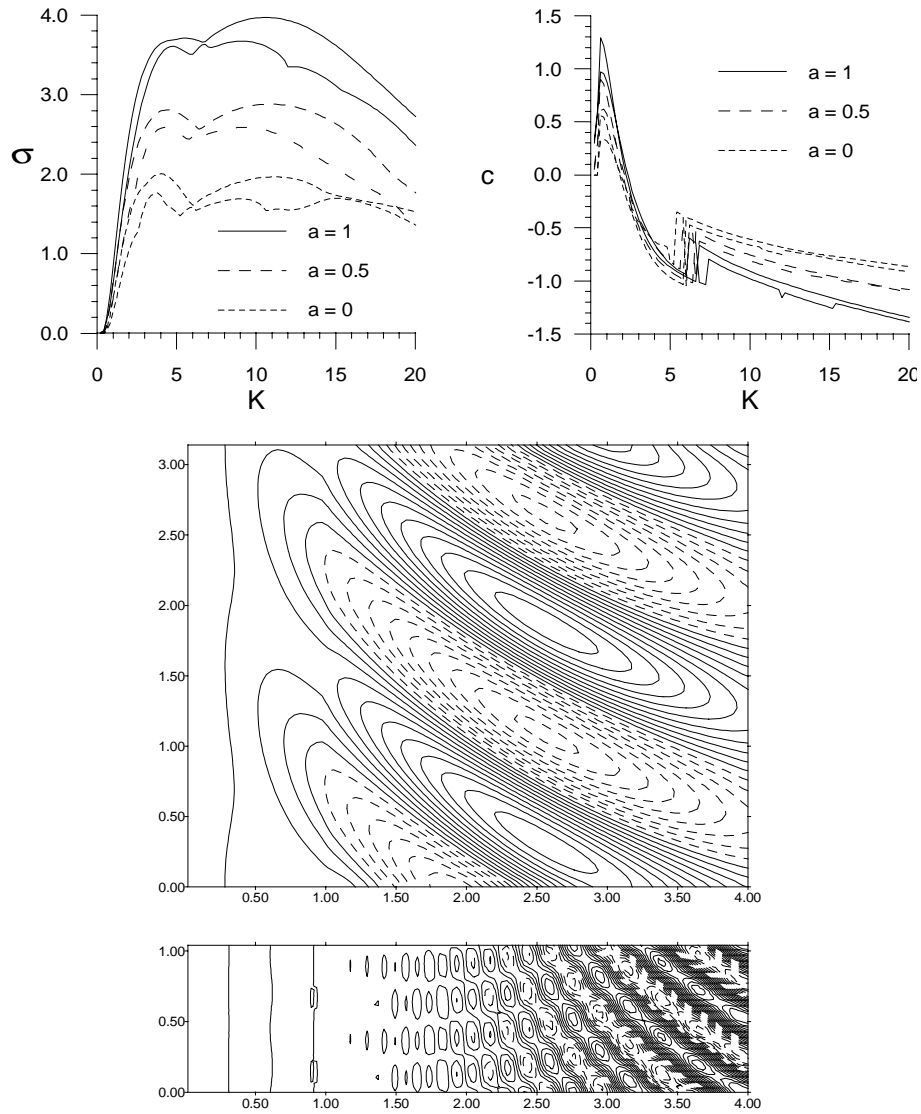


Figure 2.10: Growth rates and migration speed,  $c = -\text{Im}(\omega)/k$ , curves of the fastest growing modes as a function of the wavenumber for different values of the parameter  $a$ . All other parameter values are  $m = 3$ ,  $r = 1.5$ ,  $\hat{f} = 5.35$ ,  $\hat{\gamma} = 10^{-3}$ ,  $\beta = 0.33$ ,  $b = 0.1$  and  $V < 0$ . The upper topographic contour lines (Coriolis mode) correspond to the left relative maximum in the dominant growth rate curve. The down topographic contour lines (frictional mode) correspond to the right relative maximum in the dominant growth rate curve.

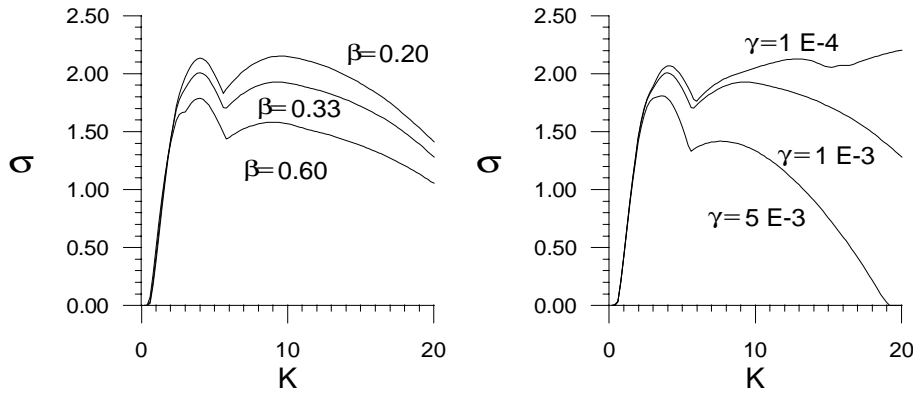


Figure 2.11: Growth rate curves of the fastest growing modes for different values of the transverse bottom slope coefficient  $\beta$  (left) and for different values of the Coulomb coefficient  $\hat{\gamma}$  (right). All other parameter values are  $m = 3$ ,  $a = 0$ ,  $r = 1.5$ ,  $\hat{f} = 5.35$ ,  $\hat{\gamma} = 10^{-3}$ ,  $\beta = 0.33$ ,  $b = 0.1$  and  $V < 0$ .

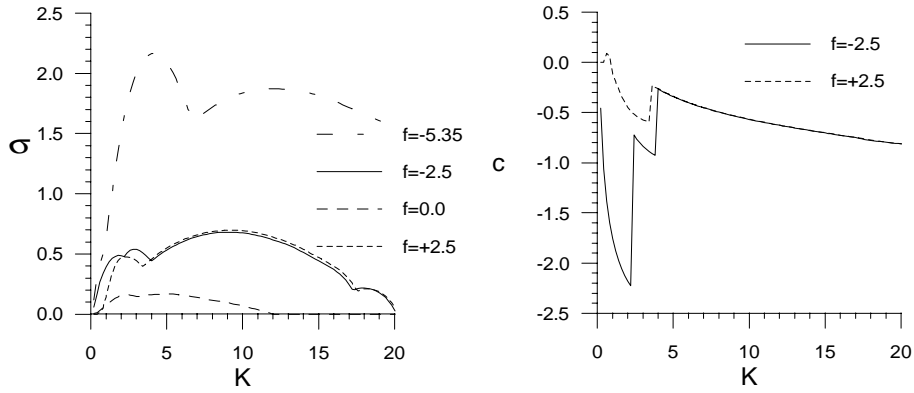


Figure 2.12: Growth rate and migration speed curves of the fastest growing modes for different values of the Coriolis parameter  $\hat{f}$ . All other parameter values are  $m = 3$ ,  $a = 0$ ,  $r = 1.5$ ,  $\hat{\gamma} = 10^{-3}$ ,  $\beta = 0.33$ ,  $b = 0.1$  and  $V < 0$ .

with  $b = 0.1$ . This is the dimensionless version of equation (2.8) discussed in section 2.1.2. The exponential decaying factor has been included in order to reproduce the finite width of coastal currents, which is due to the finite extension of the forcing by wind and by pressure gradients. Here, the choice  $b = 0.1$  has been taken. This implies that the  $e$ -folding length scale is 120 km, which seems a reasonable estimate. Results were found to be rather independent of the precise value of  $b \neq 0$ , so this parameter will not be varied in the forthcoming experiments. If  $b = 0$  is selected, spurious solutions appear because, as we will see in section 2.4, a uniform current may excite bedforms extending to infinity in case  $m > 1$ . This is incompatible with our boundary conditions at infinity which are appropriate to seek bedforms trapped to the inner shelf. In case  $m = 1$ , the finite width of the current does not need to be included explicitly into the model because, as it will be shown in section 2.4, the instability is related to the sloping bottom and, therefore, it is not active on the outer shelf. It was also found that for  $m > 1$  a larger number of collocation points is required than in the case studied in the previous subsection. All results to be shown from now on have been computed with  $N = 120$ : for larger  $N$  results differ by less than 1%.

In figure 2.10 the growth rates and migration speeds are shown as a function of wavenumber  $k$  for the cases  $a = 1$ ,  $a = 0.5$  and  $a = 0$ . All other parameters have their default values, except that  $\hat{\gamma} = 10^{-3}$  has been selected. The motivation for this change is that downslope effects in the sediment transport are more important if higher exponents in the sediment transport are considered. Growth rates decrease with decreasing values of  $a$ , as was also found in case  $a = 1$ . However, growth rates are much larger than in case  $m = 1$ . An important difference is that now two different instability

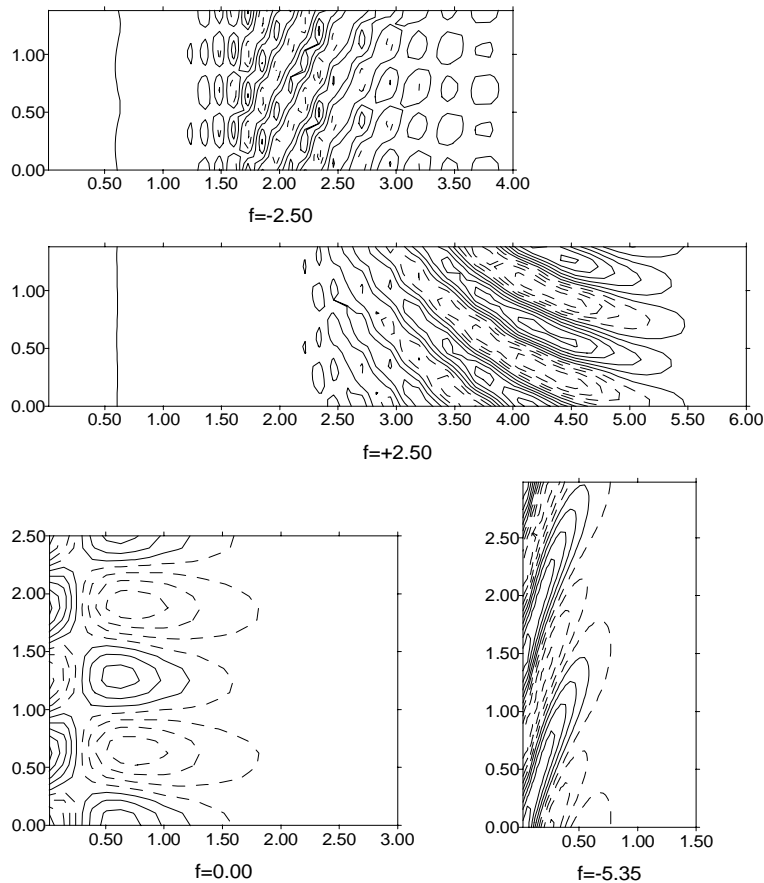


Figure 2.13: Contour plots of the preferred bed forms for  $\hat{f} = -5.35, -2.5, 0$  and  $\hat{f} = 2.5$ . Other parameter values are as in figure 2.12. For  $\hat{f} = +2.5, -5.35$  they are of the Coriolis type while for  $\hat{f} = -2.5$  it is of the frictional type.

modes appear, each of them with its own maximum in the growth rate curve. In anticipation of the discussion that will be given below, the mode with smaller dominant wavenumber will be referred to as *Coriolis mode* and the one with larger dominant wavenumber will be called the *frictional mode*. For this particular parameter set, the largest growth rate is attained by the Coriolis mode with a wavenumber  $k \sim 5.4$  (dimensional wave-length of about 14 km) and turns out to be  $\text{Re}(\omega) = 3.7$ , with a corresponding migration speed of 0.9. Using the method discussed in the previous subsection yields an  $e$ -folding time scale of approximately 800 years, which is quite a realistic value. It is remarkable that even for small values of  $a$  instabilities are found. Thus in this case the basic current needs not to be mainly driven by longshore pressure gradients: also wind effects can generate bedforms. A second remarkable difference is that migration speeds are positive for small  $k$  which means that long topographic waves move upstream. However, the modes with the largest growth rate appear to migrate downstream.

Figure 2.10 also shows the spatial structure of the preferred bedforms which is quite different from that found in the previous section. The Coriolis mode consists of elongated ridges with the seaward end of the crests shifted downstream with respect to their shoreface attachment (in this particular case; the general rule is they are cyclonically oriented with respect to the current). Moreover its wavenumber is a factor 2 smaller than those found for  $m = 1$  (compare with figure 2.2). Thus instead of shoreface-connected ridges these bedforms resemble large-scale sand banks which are usually observed further offshore. The frictional mode consists of a series of alternating shoals and pools which occur on the outer shelf and slowly decay in the seaward direction. The spatial pattern resembles that of multiple free bars in rivers (Schielen *et al.*, 1993) but in this case the bedforms have their maximum amplitude near the seaward end of the inner shelf. Even though the bedforms are not elongated ridges, a suggestion of a cyclonically oriented pattern is still apparent

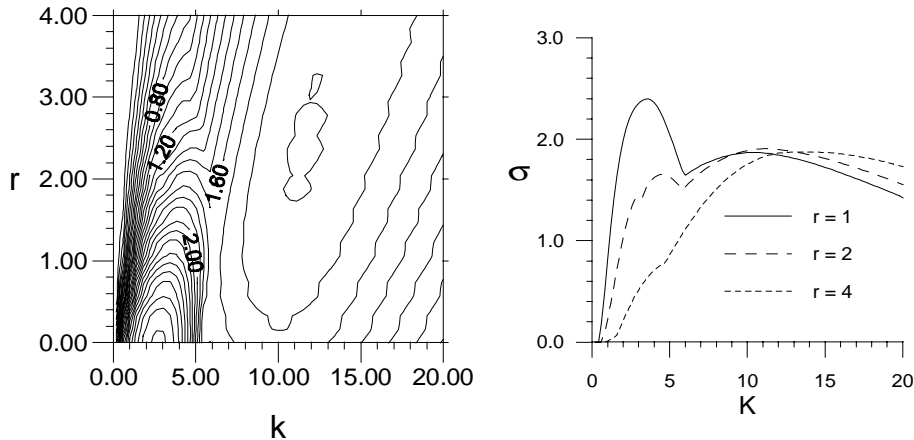


Figure 2.14: Curves of constant growth rate of the dominant mode as a function of wavenumber  $k$  and friction parameter  $r$  (left). Growth rate curves for different fixed values of  $r$  (right). A quadratic bottom friction law is adopted and parameter values are  $m = 3$ ,  $a = 0$ ,  $r = 1.5$ ,  $\hat{f} = 5.35$ ,  $\hat{\gamma} = 10^{-3}$ ,  $\beta = 0.33$ ,  $b = 0.1$  and  $V < 0$ .

through a connection between the shoals.

In figure 2.11 the dependence of the growth rate on the transverse slope coefficient  $\beta$  and on the Coulomb coefficient  $\hat{\gamma}$  is demonstrated. All other parameters have their default values; from now on we take  $a = 0$  which implies that longshore reference velocity is slowly -and exponentially- decaying in the offshore direction. An important difference with the results obtained for  $m = 1$  is that in case  $m = 3$  the instability mechanism becomes less efficient if the transverse bottom slope is increased. Furthermore, the spatial structure of the most preferred mode hardly depends on the values of  $\beta$  and  $\hat{\gamma}$ . Again, an increase in  $\hat{\gamma}$  damps the instability.

The results are now much more sensitive to the values of the Coriolis and bottom friction parameter. This can be seen from figure 2.12, which shows the growth rates and migration speeds as a function of the wavenumber for  $\hat{f} = -5.35, -2.5, 0$  and  $\hat{f} = 2.5$ , and the corresponding bedforms in figure 2.13 (results for  $\hat{f} = 5.35$  have already been shown in figure 2.10). If these results are compared with those of figure 2.8 it appears again that the model behaviour for  $m = 3$  is quite different from that in case  $m = 1$ . First of all, there are now hardly any differences in the magnitudes of the growth rates for positive  $\hat{f}$  (Northern Hemisphere) and negative  $\hat{f}$  (Southern Hemisphere). For  $|\hat{f}| > 4.3$  the preferred bedforms correspond to the Coriolis instability mode, have wave-lengths of 12 – 15 km and their crests are rotated *cyclonically* with respect to the principal current direction, i.e., anticlockwise on the Northern Hemisphere and clockwise on the Southern Hemisphere. The perturbation, both in the bathymetry and in the flow, is located close to the coastline for  $\hat{f} < 0$  and further offshore in case that  $\hat{f} > 0$ . As it will be seen in section 2.4.3, on the Southern Hemisphere the current shows no offshore deflection over the crests as in the case  $m = 1$ . However, on the Northern Hemisphere this is not clear. In contrast to the case  $m = 1$  the perturbation of the reference flow is characterized by high values of the vorticity, which are negative above the crests and positive above the troughs. Now, with decreasing values of  $|\hat{f}|$  the growth rates become smaller. If  $|\hat{f}| < 4.3$  the frictional mode is selected, which is characterized by larger wavenumber ( $k \sim 10$ , hence dimensional wave-lengths of the order of 7 km). In the section 2.4.3 it is shown that the perturbed flow diverges over the shoals and converges over the pools. A Coriolis veering superimposed on this pattern can be seen and the flow accelerates over the shoals and decelerates over the pools.

Finally we investigate the dependence of the model results on the bottom roughness. In figure 2.14 contour lines of the growth rate are shown as functions of the wavenumber  $k$  and friction parameter  $r$ . Similarly to the case  $m = 1$  we find instability for all values of  $r$ . Here, instability is favoured for small  $r$  and small  $k$  (lower left corner of the figure) or by large values of  $r$  and  $k \sim 10$  (upper and middle part of the figure). Thus we obtain two instability regions with a transition between them for about  $k \sim 6$  and  $r \sim 0.5$ . In the region corresponding to large values of  $r$ , the dominant instability mode is the frictional one. This is the reason why we have called it this

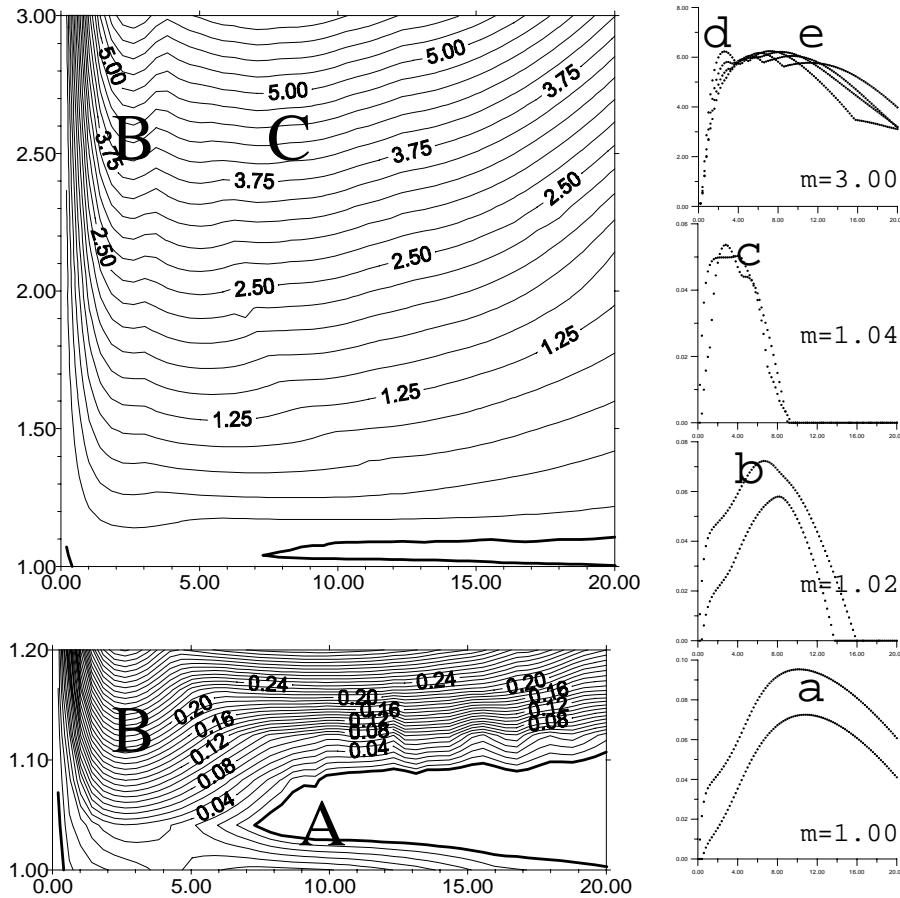


Figure 2.15: Left up: Curves of constant  $\text{Re}(\omega)$  as a function of wavenumber  $k$  and exponent  $m$  in the sediment transport parametrization. Left down: Enlargement of the upper left figure near  $m=1$ . Figures on the right: growth rate curves for different, but fixed, values of  $m$ .

way. On the other hand, in the region for small values of  $r$ , the Coriolis mode is dominant. Since in this case the crests are cyclonically rotated with respect to the current direction and growth rates increase with increasing  $|\hat{f}|$ , this instability mode seems related to earth rotation effects and therefore, it has been called Coriolis mode. The properties of the perturbations in case of Southern Hemisphere flow (not shown) are qualitatively similar. An interpretation of these results will be given in section 2.4.

### 2.3.4 Exploration with respect to $m$

Since the solutions of the model for  $m = 1$  and for  $m = 3$  are fundamentally different it is interesting to investigate how the model behaviour evolves from  $m = 1$  to  $m = 3$ . Therefore, such an exploration for  $1 < m < 3$  is carried out. The depth profile is given by equation (2.16) and the current profile is chosen to be

$$V(x) = \begin{cases} -[1 + a\beta x] & \text{if } 0 \leq x \leq 1 \\ -[1 + a\beta] \exp(-b(x-1)) & \text{if } x \geq 1 \end{cases}$$

with  $b = 0.05$ . The choice of the current profile implies that the model is considered for a *linear* bottom friction. This seems desirable since profiles significantly different from that considered in section 2.3.2 rule out upcurrent oriented oblique ridges. However, for  $m > 1$ , some velocity decay far offshore is necessary in order that the model equations have solutions which verify the boundary conditions at infinity. This will be explained in section 2.4 while analyzing the physical mechanisms underlying the model. As we will see a posteriori, this current profile allows us to investigate the

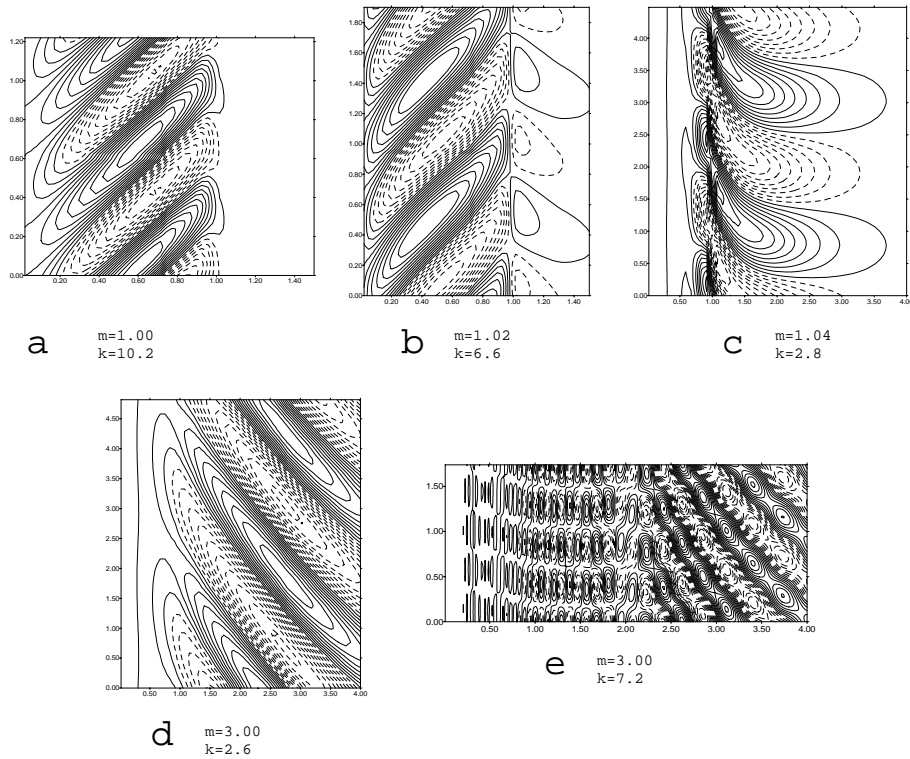


Figure 2.16: Contour plots of preferred bedforms related to the different locations as indicated in plots on the right in figure 2.15

competition between the different instability sources within the model. Furthermore, we select  $V < 0$  and select the parameter values:  $a = 1$ ,  $r = 1.5$ ,  $\hat{f} = 5.35$ ,  $\hat{\gamma} = 10^{-4}$  and  $\beta = 0.33$ .

Figure 2.15 shows  $\text{Re}(\omega)$  as a function of  $m$  and wavenumber  $k$ . Three instability regions are found, indicated by the letters A, B and C in the figure. The first one occurs for small values of  $m$ , very close to 1, and large wavenumbers,  $k \sim 10$ . Bedforms in this region are typically upcurrent oriented oblique ridges (see figure 2.16). For  $m$  close to 1 a strong sensitivity to variations of this exponent is found. For  $m = 1.02$  (plot b of figure 2.16), the upcurrent oblique ridge behaviour is still very pronounced. In contrast, for  $m = 1.04$  bedforms have changed drastically (plot c) as they are cyclonically oriented bars which extend well on the outer shelf. The second instability region, B, occurs for higher values of ( $m \sim 1.1 - 3$ ) and for small wavenumbers  $k \sim 3$ . It corresponds to cyclonically oriented ridges over the shelf (plot d of figure 2.16), similar to those shown in figure 2.10. Finally, the instability region C is characterized by  $m \sim 1.5 - 3$  and  $k \sim 6$ . The corresponding bedforms are series of shoals and pools (plot e). After comparison with the instability regions discussed in the last paragraph of section 2.3.3, it seems that region B is dominated by the Coriolis force while region C is dominated by the frictional force. In summary, upcurrent oriented ridges dominate for  $m$  very close to 1, but as soon as  $m$  is slightly increased, either the Coriolis mode bedforms or the frictional mode bedforms dominate, depending of the magnitude of the wavenumber.

## 2.4 Physical mechanisms

### 2.4.1 Introductory remarks

In this section the physical mechanisms will be discussed which are responsible for the growth and observed characteristics of the morphologic features in our model. For this purpose it is useful to combine the continuity equation (2.10) and the bottom evolution equation (2.11). The result is

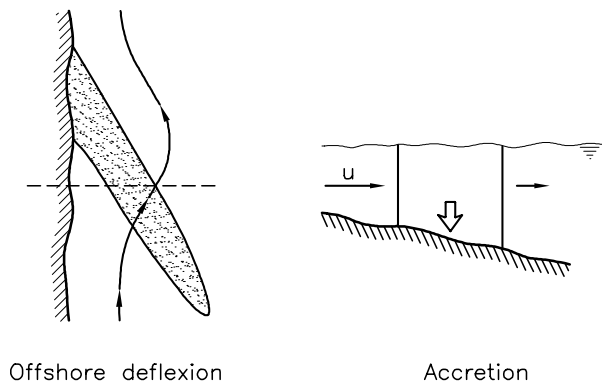


Figure 2.17: Schematic view of the transverse bottom slope mechanism. An upcurrent oriented ridge produces offshore deflexion of the flow. Then, flow into deeper water must converge so that a sediment convergence occurs over the ridge.

(in the quasi-steady limit  $\epsilon \rightarrow 0$  and for a Froude number  $F \rightarrow 0$ )

$$\begin{aligned} \frac{\partial h}{\partial t} + \frac{mq_0}{H} \frac{V}{|V|} \frac{\partial h}{\partial y} - \frac{\partial}{\partial x} \left( \hat{\gamma} q_0 \frac{\partial h}{\partial x} \right) - \frac{\partial}{\partial y} \left( \hat{\gamma} q_0 \frac{\partial h}{\partial y} \right) = \\ \frac{q_0}{|V|} \left( \frac{m}{H} \frac{dH}{dx} - \frac{(m-1)}{V} \frac{dV}{dx} \right) u + (m-1) \frac{q_0}{|V|} \frac{\partial u}{\partial x} \end{aligned} \quad (2.17)$$

where  $q_0 = |V|^m$ . On the left-hand side an advective contribution and two diffusive terms appear. Thus, in absence of the right-hand side, this equation would describe just migrating and decaying bedforms. The principle sources for instability appear on the right-hand side. The first term only acts in case there is a transverse sloping reference bottom. The last two terms are only active in case  $m > 1$  (i.e., a 'faster than linear' sediment transport parametrization). They are related to the cross-shore shear of the basic current profile and the divergence of the offshore flow component, respectively. In the next subsections the dominant instability mechanisms will be discussed.

## 2.4.2 Transverse bottom slope mechanism

Consider the first term on the right-hand side of equation (2.17). It shows that an offshore deflection over a bar on a transverse sloping reference bottom is related to morphologic instability. The mechanism can be studied in isolation by selecting  $m = 1$ , as was done in section 2.3.2. The positive feedback between flow and bottom in this case can be understood by considering a control volume at a crest (where  $\partial/\partial y = 0$ ) with vertical sides parallel and perpendicular to the coast (see figure 2.17). In case of an offshore flow component ( $u > 0$ ) the mass deficit caused by the movement of the column into deeper water must be compensated by a convergence of the flow. As in case  $m = 1$  the sediment flux,  $\mathbf{q}$ , is proportional to the velocity of the current, there will be convergence of sediment above the crests and thus the ridges will grow. Note that this convergence is even more effective on the downstream side of the ridge because the longshore movement of the control volume causes an additional mass deficit in this area. On the upstream side of the ridge the flow convergence is counteracted by this effect. This explains the downstream migration of the bedforms. The reason that the bars are trapped to the inner shelf is that in this area the transverse slope is much larger than that on the outer shelf. This mechanism was first described by Trowbridge (1995).

The deflection of the alongshore current over a ridge is a consequence of mass conservation which can be seen as follows. Consider a steady constant flow in an open sea with constant depth. Next introduce an isolated and elongated sand bank of which the crest has an angle with the direction of the undisturbed current. Then, if  $\xi$  is the cross-bank coordinate,  $v_\xi$  the cross-bank component of the current and  $D$  the total depth, the continuity equation for small Froude number equation reads  $\partial(Dv_\xi)/\partial\xi = 0$  because there are no variations in the along-bank direction. Therefore, a decrease in  $D$  will produce an increase in  $v_\xi$ . Now assume for the moment that the flow is irrotational, as was done by Trowbridge (1995). In that case the alongbank flow component remains constant and

consequently the current will veer towards the crest. Application of this argument to our model geometry yields that upcurrent oriented bars will induce an offshore deflection of the current over the crests and downcurrent bars will cause an onshore deflection over the crests. This implies that instability only occurs if the seaward ends of the ridges are shifted upcurrent with respect to their shoreface attachments. In appendix C a simple model is discussed which allows for approximate analytical solutions of the eigenvalue problem for  $m = 1$ , irrotational flow and small bottom slopes. These solutions confirm the statements just described.

Finally we remark that the transverse slope mechanism also strongly depends on the selected basic current profile. In particular, if parameter  $a = \delta/r$  is reduced the growth rates become substantially smaller and preferred modes with a different spatial structure are found. This appears to be related to the presence of the second term on the left-hand side of equation (2.17). If  $a = 1$  this contribution just describes a downcurrent migration of bedforms with (in case  $m = 1$ ) a constant celerity  $V/H$ . However, if  $a$  is reduced the celerity decreases in the offshore direction and apparently this suppresses the instability.

### 2.4.3 Vorticity mechanisms: role of bottom friction and Coriolis

The results of sections 2.3.3 and 2.3.4 indicate that in case a 'faster than linear' sediment transport (i.e.,  $m > 1$ ) is considered, the preferred bedforms differ substantially from the case that  $m = 1$ . The principle reason for these qualitative changes is that the term

$$(m-1) \frac{q_0}{|V|} \frac{\partial u}{\partial x}$$

in equation (2.17) becomes an important source of morphologic instabilities while, according to numerical simulations, for  $m > 1.05$  the transverse slope mechanism is not active anymore.

The mechanism appears to be related to the production of vorticity by bottom frictional and Coriolis torques, combined with the advection of vorticity by the background current. Hence, in this case the presence of vorticity is a necessary condition for instability. It can be studied in isolation by assuming a flat bottom ( $H = 1$ ) and a uniform current ( $|V| = 1$ ). These parameter values will be used in the rest of this section.

Clearly, according to equation (2.17), the mechanism describes exponentially growing bedforms in case the cross-shore flow component at the bar crest increases in the seaward direction. This can be understood as follows: from the continuity equation (2.10) it follows that in case of a flat reference bed the flow above a crest is free of divergence. Using the parametrization of the sediment flux it then follows that at the crest

$$\nabla \cdot \mathbf{q} \equiv |V|^{m-1} \left[ \frac{\partial u}{\partial x} + m \frac{\partial v}{\partial y} \right] = -|V|^{m-1} (m-1) \frac{\partial u}{\partial x}$$

where in the last step the continuity equation has been used. Thus a net sedimentation at the bar crest indeed requires  $\partial u/\partial x > 0$  and a faster than linear transport.

To analyze the nature of the instability process we should now investigate how friction and Coriolis forces affect the flow adjustment to some particular bedforms and how they make  $\partial u/\partial x$  to be positive at the crests. To this purpose it is again useful to consider the vorticity balance. For the present model setting (including a quadratic bottom friction) it reads

$$V \frac{\partial \Omega}{\partial y} + \hat{f} \left[ \frac{\partial u}{\partial x} + \frac{\partial v}{\partial y} \right] = -r\Omega - r \frac{\partial v}{\partial x} + \delta \frac{\partial h}{\partial x} \quad (2.18)$$

where  $\Omega = \partial v/\partial x - \partial u/\partial y$  is the relative vorticity. As can be seen there are three sources of vorticity production, which are related to planetary vortex stretching and to frictional torques.

For the moment we will assume that earth rotation effects are absent. Then, motivated by the results of section 2.3.3, we will study the response of the system with a background flow  $V = 1$  to bottom perturbations of the form  $h = \cos px \cos ky$ . This represents a series of alternating shoals and pools in both the longshore and cross-shore direction. In case  $r = \delta = 0$  there is no vorticity production so that the flow is irrotational. Consequently, streamlines will diverge in the upstream part of the bars, converge on the leeside and be nondivergent at the crest, see figure 2.18(left).

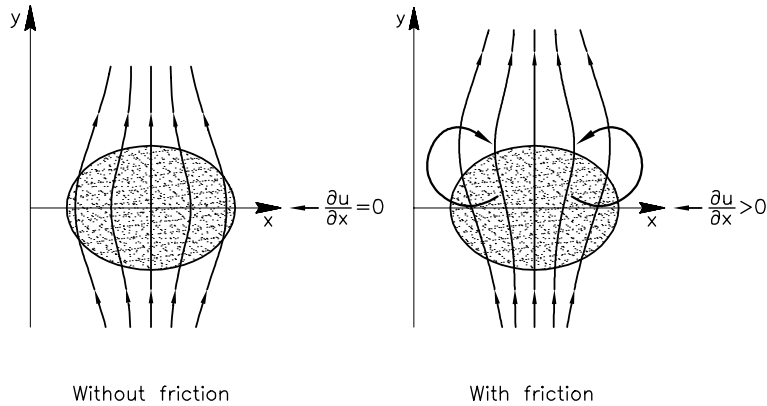


Figure 2.18: Schematic view of the bottom friction mechanism. In case of sediment transport faster than linear,  $m > 1$ , convergence of sediments means  $\partial u/\partial x > 0$ . In absence of bottom friction, streamlines over a round shoal diverge at the upflow side and converge at the lee. Bottom frictional torques generate vorticity which makes the streamlines to diverge at the top with the result that now deposition over the top occurs.

This can be derived from the equations of motion for the perturbed flow, which for the present conditions reduce to

$$\frac{\partial v}{\partial x} - \frac{\partial u}{\partial y} = 0 \qquad \frac{\partial u}{\partial x} + \frac{\partial v}{\partial y} - \frac{\partial h}{\partial y} = 0$$

For the given bottom perturbation it follows that the cross-shore flow component  $u$  has a  $90^\circ$ -phase shift with respect to  $h$ . Consequently, the quantity  $\partial u/\partial x$  is zero at the crest of the bar, hence there is no growth, but only a migration of bedforms.

Now assume that  $r \neq 0$  and  $\delta < 0$  (negative because the flow  $V > 0$  in this case). Since the frictional forces in the  $y$ -direction are larger in smaller water depth torques are exerted on the water parcels. These torques can be recognized as the last two terms in equation (2.18) and they act in the same way. Over a shoal they cause the production of positive vorticity on the right-hand side and negative vorticity on the left-hand side, see figure 2.18(right). Advection of this vorticity by the background flow then results in a clockwise circulation on the left-hand side of the downstream region of the bar. Similarly an anticlockwise circulation appears on the right-hand side. Superimposing this secondary flow field on that of the irrotational flow yields streamlines which diverge at the crest, see figure 2.18(right). Thus at this location  $\partial u/\partial x > 0$  and the bedforms will grow.

The class of bottom modes which is explained by this frictional mechanism corresponds to region C in the upper left plot of figure 2.15. Examples of the corresponding spatial patterns are shown in figure 2.10 and figure 2.13 (cases  $f = 0$ ,  $f = \pm 2.5$ ).

The obvious fact that this mechanism does not need a sloping bottom makes it to generate a patch of shoals and pools which extends seaward to infinity if the current does so. This causes problems in the numerical model where the boundary condition imposed forces bottom perturbations to decay far from the coast. Therefore in case  $m > 1$  a background flow was needed which vanishes at large distances from the shore.

It is also interesting to study the situation that earth rotation effects play a dominant role in the vorticity balance. They are the principle cause for the presence of the instability region in figure 2.14 for  $m = 3$  and small values of the friction parameter (region B in figure 2.15). The resulting eigenfunctions describe elongated bedforms of which the crests are cyclonically rotated (anticlockwise on the Northern Hemisphere) with respect to the principal current direction, see figure 2.10. To understand this process we will analyze the flow response to a series of such ridges, modelled as  $h = \cos(px + ky)$ . Again a flat bottom and a uniform background current will be assumed and the friction parameter is now  $r = 0$ .

In case that  $\hat{f} = 0$  the flow is irrotational and its streamlines for  $V = 1$  are sketched in figure 2.19. Note that the cross-shore flow component has a  $90^\circ$  phase shift with respect to the bottom perturbations, hence  $\partial u/\partial x = 0$  at the crests and there is only migration of the bedforms.

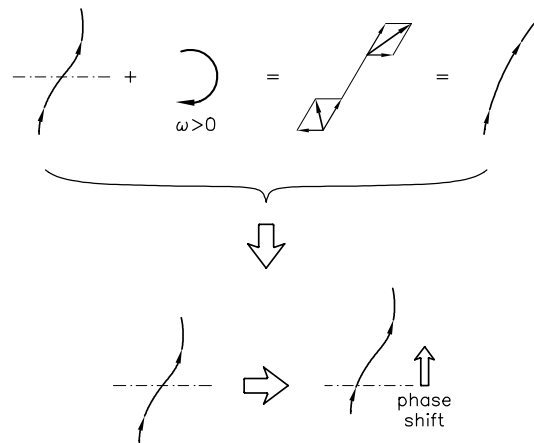
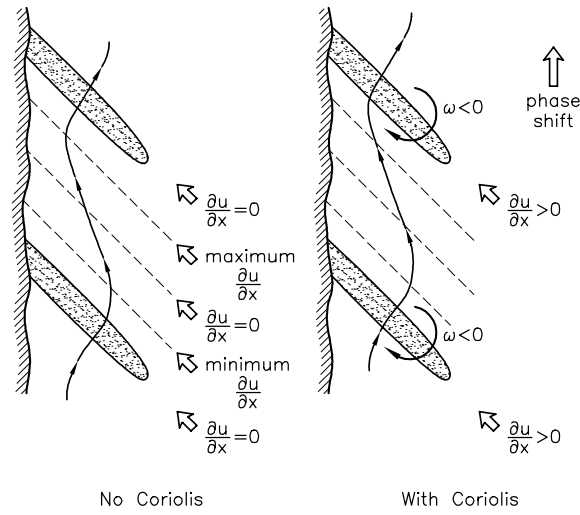


Figure 2.19: Schematic view of the Coriolis mechanism. Up: the flow pattern over a system of cyclonically oriented ridges in absence of Coriolis force has  $\partial u/\partial x = 0$  at the crests. Coriolis torques induce an anticyclonic vorticity over the crests which makes the flow pattern to shift downstream. Hence,  $\partial u/\partial x$  is now positive over the crests which results in deposition over the crests. Flow over anticyclonic oriented ridges behaves just in the opposite way. Down: the anticyclonic vorticity superimposed to the flow pattern which would occur in absence of Coriolis produces a downcurrent shift of the flow.

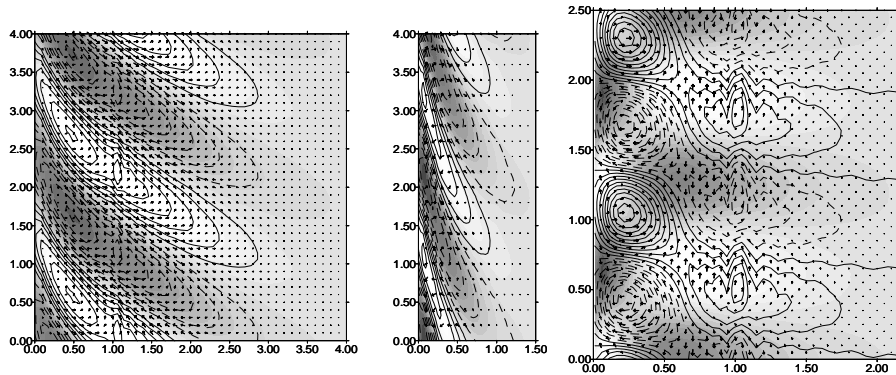


Figure 2.20: Vorticity distribution along with perturbed topography and perturbation on the current for  $m = 3$ ,  $a = 0$ ,  $\hat{\gamma} = 10^{-3}$ ,  $\beta = 0.33$  and  $b = 0.1$ . Continuous and dashed lines mean anticyclonic and cyclonic vorticity, respectively. Perturbation of the current indicated by arrows and shoals and pools are indicated by dark and white colours, respectively. From left to right, Coriolis mechanism ( $r = 0$ ,  $\hat{f} = 5.35$ ), on the left  $V < 0$  and on the middle  $V > 0$ ; and bottom friction mechanism ( $r = 1.5$ (quadratic),  $\hat{f} = 0$ ) and  $V < 0$  - $V > 0$  gives the same pattern but symmetrical with respect to the  $x$  axis.

Next assume that  $\hat{f} > 0$  and use the fact that the potential vorticity of the flow, defined in the present case as  $(\Omega + \hat{f})/(1 - h)$ , is conserved for individual fluid particles. The relative vorticity  $\Omega$  is zero at the locations where  $h = 0$ , thus if the flow moves into the upstream region of a bar negative relative vorticity will be produced. Likewise, in the downstream region of the bar positive vorticity is generated. Advection of this vorticity (see the first term in equation (2.18)) causes a clockwise circulation around the crest of the bar. As is shown in figure 2.17, this produces a downcurrent shift of the perturbed flow pattern with the result that  $\partial u/\partial x$  becomes now positive on the crests. It can be seen that in case of anticyclonically oriented ridges the flow behaves just in the opposite way, i.e., Coriolis torques make  $\partial u/\partial x$  to be negative over the crests.

The spatial correlation between the bedforms and the vorticity field is illustrated in figure 2.20 for both  $V = 1$  and  $V = -1$ . Note that the vorticity distribution and bedforms related to the Coriolis mechanism differ from those found in case the frictional mechanism is dominant (figure 2.20). The reason is that bottom frictional torques have the same sign in the upstream and downstream region of the bar, so that inertial effects cause the centre of vorticity to be shifted to the lee side. On the contrary, Coriolis torques change sign when water parcels move over the crest and advection results in a centre of vorticity at the crest. This forces the preferred bottom modes in both cases to have different spatial structures.

## 2.5 Conclusions

The main objective of the present study was to obtain a better understanding of the presence and characteristics of shoreface-connected sand ridges, as observed on the inner shelf of some coastal seas. It was argued that such large-scale bedforms are formed due to a positive feedback between the water motion and the erodible bottom. The hypothesis has been studied in the framework of a depth-integrated shallow water model, supplemented with a sediment transport parametrization and a bottom evolution equation. It extends an earlier model developed by Trowbridge (1995) in the sense that Coriolis and bottom frictional forces are included. Moreover, the sediment transport is assumed to be proportional to some power  $m$  of the flow velocity and the tendency of the flux to have a downslope component has been taken into account.

The background of the model is a basic state which is uniform in the direction parallel to the coast. It describes a steady mean longshore flow, driven by wind and a pressure gradient, over a reference topography. Only the averaged component of the forcing is considered, namely, weather fluctuations in wind stress and pressure gradient are discarded. Some of the implications of this simplification have been sketched in appendix A. The stability properties of this morphodynamic equilibrium with respect to small bottom perturbations, which are rhythmic in the longshore di-

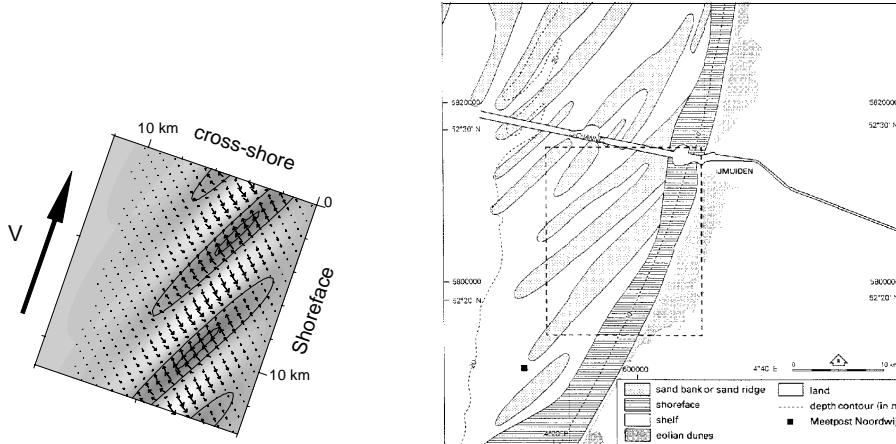


Figure 2.21: A comparison of modelled ridges (left) against observed ridges off the Dutch coast (right) after Van de Meene (1994). Crests are in dark and troughs in white. The direction of the mean current is indicated by a big arrow while the perturbation on this current associated to the ridges is indicated by small arrows. Model parameters:  $m = 1$ ,  $a = 1$ ,  $r = 1.5$ ,  $\hat{f} = 5.35$ ,  $\hat{\gamma} = 10^{-4}$ ,  $\beta = 0.33$  and  $V < 0$ . Note that the scale of the plot on the left is approximately two times larger than the plot on the right.

rection, have been investigated. A systematic analysis of the model has revealed that inherent morphologic instabilities indeed develop and that their properties strongly depend on the model parameters.

In case  $m = 1$  the dominant bedforms are trapped to the inner shelf and have an upcurrent rotated orientation, i.e., the seaward ends of the crests are shifted upstream with respect to their shoreface attachments. The growth rate and longshore wave-length are largely determined by the relative contribution of wind and the longshore pressure gradient in the maintenance of the background current. In case the latter effect dominates the model results show good agreement with field data, e.g. in case of the Dutch inner shelf a spacing of about 7 km is obtained (see figure 2.21). With increasing wind effects the growth rates become smaller and the wave-lengths increase. Coriolis and bottom friction also affect the instability mechanism, but they do not induce significant qualitative changes. Physically, the bedforms are due to the transverse sloping bottom mechanism and their formation is associated with an offshore current deflection over the bars. It has been demonstrated that these characteristics can be understood from mass conservation of both the water and the sediment. The mechanism is effective only for  $1 \leq m < 1.05$ .

It should be noted that the agreement between the predicted spacing of the ridges and the observed spacing off the Dutch coast depends on the choice of the bedslope coefficient in the sediment transport,  $\gamma = 0.08$  (similar values,  $\gamma \sim 0.1$ , give a good fit for the American ridges, Parra (1999)). However, even though the precise values of  $\gamma$  are rather uncertain, this value is too small compared to the usually accepted values which are  $\gamma \sim 1$ . It can be seen in appendix A, equation (A.2), how taking into account a non-uniform wave orbital velocity near the bottom may change the effective value of the bedslope coefficient. Preliminary calculations with this parametrization indicate that the value of  $\gamma$  needed to fit the observed spacing tends to increase towards more realistic values. In other words, if  $\gamma \simeq 1$  is chosen in this case, a spacing of  $\lambda \simeq 12 \text{ km}$  is obtained. Even though the discrepancy is not too big, further attention should be paid to this issue for future research. It is also worth mentioning that, for simplicity, the present model assumes a uniform wave stirring coefficient  $\nu$ . The statistical approach sketched in appendix A allows for a non-uniform wave stirring. Preliminary computations in case of a seaward decreasing  $\nu$  show some quantitative changes but not essential qualitative modifications of the bedforms.

If a larger exponent  $m$  in the sediment flux is considered other types of bottom modes are obtained. In general they do not resemble the observed shoreface-connected ridges. For large values of the friction parameter a pattern of alternating shoals and pools is found which extends over both the inner and outer shelf. For realistic parameter values the spacings are of the order of 5 – 10 km. The formation of these bedforms can be understood as being a consequence of vorticity

production by frictional torques. If the bottom roughness becomes small more elongated bedforms appear, with spacings of order 15 km, of which the crests are rotated cyclonically with respect to the current direction. Their formation is related to the production of vorticity by Coriolis torques.

It appears that the best comparison between model results and observed shoreface-connected ridges is obtained in case  $m = 1$ . This constraint can be seen as a limitation of the model. However, it is also plausible that it gives a clue on which are the environmental conditions that lead to the occurrence of such ridges. Thus, the  $m = 1$  condition suggests that ridges mainly form during stormy conditions, during which the waves stir the sediment which is subsequently transported by the mean current. A further condition is that the ratio  $V/H$  is almost constant, where  $V$  is the background current and  $H$  the equilibrium bottom profile, which is realistic if the background flow is mainly controlled by a longshore pressure gradient and not by the windstress.

On the other hand these statements may be a gross simplification of reality. As can be seen from figure 1 in Swift & Field (1981) or figure 1 in Parker *et al.* (1982) the observed patterns of shoreface-connected ridges are rather complex and the elongated shape and upcurrent orientation are only indicative of the mean characteristics. Many ridges have secondary shoals (see e.g. figure 4 in Swift *et al.*, 1978) which suggests that also the frictional vorticity mechanism might play a modifying role in the dynamics. As it has been shown in section 2.3.4, its effect can not be included by choosing a value for  $m$  slightly larger than 1, since in this case the transverse slope mechanism is no longer effective. It seems preferable to specify a storm climatology and run the model partly in the  $m = 1$  mode and partly in the  $m = 3$  mode. In principle this is a difficult problem because it requires the use of different velocity profiles and different velocity amplitudes for both situations.

It is important to realize that observed shoreface-connected ridges on the inner shelf are finite amplitude features while the present analysis only yields information on their initial formation. Thus, a challenging issue is to perform a nonlinear finite amplitude analysis of the ridge behaviour. This would lead to a prediction of the amplitude of the ridges, which cannot be extracted from the present linear analysis. This kind of non-linear modeling is done in chapter 4

Finally, remark that tidal oscillations are not considered in the present study. However, the present study shows that shoreface-connected ridges have an entirely different origin. Indeed, tidal sand banks are associated to a  $m > 1$  power in the sediment transport and to earth rotation (Hulscher *et al.*, 1993). It has been shown in sections 2.3.3 and 2.3.4 that even in the proximity of the coast, bedforms for  $m > 1$  are cyclonically oriented. On the other hand, the correct orientation is obtained only if  $m \simeq 1$  and is not affected by Coriolis. Nevertheless, it is conceivable that tidal currents affect the ridges in some way. First, the mean steady current in the present model can be considered to be partially driven by a residual component in tidal forcing. This could be assimilated to a pressure gradient-type forcing, reinforcing or opposing the effect of the alongshore slope in the sea surface. Second, the tidal oscillation itself can be incorporated in the morphodynamic model. To this end, an important extension of the present model consists in the assumption of a basic undisturbed current with a steady component plus an oscillatory one (tidal). This type of modelling is done in chapter 3.

